Synchrotron radiation X-ray microtomography for the visualization of intra-cochlear anatomy in human temporal bones implanted with a perimodiolar cochlear implant electrode array

Fergio Sismono,[a]* Lucia Mancini,[b] Marc Leblans,[a] Jana Goyens,[c] Glynnis De Greve,[a] Sara Schneiders,[a] Karen Beckers,[a] Joris Dirckx,[d] Bert De Foer[e] and Andrzej Zarowski[a]

[a]European Institute for ORL-HNS, GZA Hospitals Antwerp, Oosterveldlaan 24, Wilrijk, Antwerp 2610, Belgium, [b]Elettra Sincrotrone Trieste S.C.p.A., S.S. 14 Area Science Park, 34149 Basovizza, Trieste Italy, [c]Department Biology, Lab Functional Morphology, University of Antwerp, Universiteitsplein 1, Wilrijk, Antwerp 2610, Belgium, [d]Laboratory of Biomedical Physics, University of Antwerp, Groenenborgerlaan 171, Antwerp 2020, Belgium, and [e]Department of Radiology, GZA Hospitals Antwerp, Oosterveldlaan 24, Wilrijk, Antwerp 2610, Belgium. *Correspondence e-mail: fergio.sismono@gza.be

Recently, synchrotron radiation computed microtomography (SRµCT) has emerged as a promising tool for non-destructive, *in situ* visualization of cochlear implant electrode arrays inserted into a human cochlea. Histological techniques have been the 'gold standard' technique for accurate localization of cochlear implant electrodes but are suboptimal for precise three-dimensional measurements. Here, an SRµCT experimental setup is proposed that offers the benefit of a high spatial and contrast resolution (isotropic voxel size = 4.95 µm and propagation-based phase-contrast imaging), while visualizing the soft-tissue structures and electrode array of the cochlear implant simultaneously. In this work, perimodiolar electrode arrays have been tested, which incorporate thick and closely spaced platinum–iridium contacts and wiring. These data can assist cochlear implant and hearing research, can be used to verify electrode segmentation techniques for clinical computed tomography or could be utilized to evaluate cochlear implant electrode array designs.

1. Introduction

Cochlear implants (CIs) are medical devices that restore hearing and speech understanding in moderate to profoundly deaf patients who are unable to receive adequate benefit from conventional hearing aids. CIs directly stimulate the auditory nerve through an electrode array inserted in the cochlea. Using a microphone and an external speech processor, sounds are captured from the environment and transformed into electrical signals that are distributed over the electrode contacts of the implanted electrode array. Each contact carries the information corresponding to a specific acoustic frequency band and electrically stimulates the target auditory neurons within the cochlea. In this way, the whole speech-related frequency spectrum of captured sound can be conveyed to the auditory system.

The position of the CI electrodes with respect to the anatomical structures in the cochlea varies as a result of the surgical procedure and is of importance for the final hearing outcome of the CI recipient. For instance, the final performance on speech recognition tests is significantly better when the electrodes are implanted into the scala tympani, the inferior partition of the cochlear duct, rather than the scala vestibuli, the superior partition (Holden *et al.*, 2013; Shaul *et*

short communications
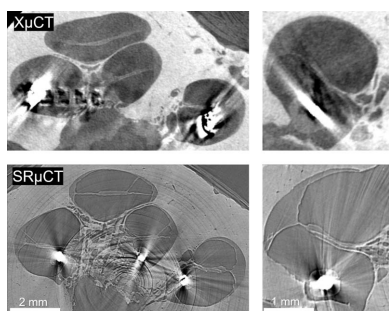
al., 2018). Also, various studies suggest that CI patients have improved audiological outcomes when the electrode contacts are positioned in close proximity to the auditory nerves in the cochlear medial wall, compared with when the contacts are positioned further away (Holden *et al.*, 2013; Chakravorti *et al.*, 2019).

A detailed investigation of the spatial relation between the electrode contacts and the neural target structures and how this affects hearing outcomes would be of great scientific and clinical interest. However, the accurate localization of the CI-electrode remains a significant challenge that has not yet been overcome. In clinical computed tomography (CT), cochlear microstructures, such as the basilar membrane, the osseous spiral lamina and Rosenthal's canal – the structure that contains the auditory nerve cell somas and is assumed to be the primary neural target region for electrical stimulation (Kawano *et al.*, 1998) – are invisible. This is due to the small differences in X-ray attenuation coefficients between soft-tissue and fluids within the cochlea combined with the high structural density of the surrounding temporal bone. Moreover, the electrode contacts, which are made out of a platinum–iridium alloy, absorb a great portion of the incident X-ray beam, which results in streaking artefacts in the final reconstructions (Saeed *et al.*, 2014).

The current 'gold standard' for accurate localization of the CI-electrode is *ex vivo* histological sectioning, but this requires extensive and complicated sample preparations, introduces processing artefacts, is destructive, time consuming and costly (Rau *et al.*, 2013; Johnson *et al.*, 2014; Iso-Mustajärvi *et al.*, 2017). Another critical limitation of histological techniques is that the spatial resolution in the longitudinal plane tends to be relatively low compared with that of the transversal plane, due to the technical constraints imposed by the serial grinding of the sample (Sun *et al.*, 2002; Rau *et al.*, 2013). This limits the maximally achievable accuracy when performing three-dimensional measurements.

Recently published findings suggest that synchrotron radiation computed microtomography (SRμCT) may be a suitable alternative to conventional histological techniques. While SRμCT has been shown to be capable of visualizing intra-cochlear soft-tissue structures with near-histological quality, it is able to generate a 3D, high isotropic spatial resolution view of the specimen, which makes it particularly suitable for precise measurements. In addition, it is non-destructive, greatly more time-efficient and requires only minimal sample processing (Elfarnawany *et al.*, 2017; Iyer *et al.*, 2018; Schart-Morén *et al.*, 2019). In recent work, the first SRμCT data on human temporal bones implanted with a clinically representative CI electrode were presented, which showed promising results in terms of visualizing intra-cochlear structures (Rohani *et al.*, 2018; Li *et al.*, 2019). However, further investigation is still necessary to assess the benefits SRμCT could provide over conventional methods.

Up to now, only cochleas implanted with lateral wall CI-electrode arrays, which incorporate relatively thin electrodes, have been investigated. Here, we present data from our recent experiment where we tested perimodiolar electrode arrays.

These types of electrode arrays are commonly used in CI surgery, as they are pre-curved in the fabrication process to take a position closer to the auditory neurons in the cochlear medial wall, which is, in turn, assumed to offer the benefit of improved audiological outcome. However, such electrodes also typically incorporate relatively thick platinum contacts that are more closely spaced together, which poses a major challenge even for SRμCT imaging. The aim of this study was to develop an experimental protocol for visualizing perimodiolar electrode arrays *in situ* with SRμCT and to assess whether it would be possible to measure the distance from the surface of the electrode contacts to neural structures.

2. Materials and methods

2.1. Sample preparation

A total of eight human temporal bones were used in this study. All samples were excised from cadaveric head specimens that were donated to the European Institute for Otorhinolaryngology in Antwerp (Belgium) for scientific and educational use. The temporal bones were fixated in a 4% formaldehyde-buffer solution. To accommodate the size restrictions imposed by the experimental setup employed, samples were trimmed manually with a drill bit to include only the cochleovestibular system, leaving a few millimetres of surrounding bone. This process resulted in a set of specimens that were each approximately 20–30 mm in length and 20–25 mm in diameter (Fig. 1). Prior to tomographic scanning, the samples were dehydrated for approximately 12 h in air. Draining of the liquid inside the cochlea was achieved by carefully placing the samples on a piece of paper tissue with the round window oriented downward. No additional pre-processing steps such as decalcification or sample staining were performed.

2.2. Cochlear implantation

Seven out of eight temporal bone samples were implanted with a CI-electrode array and one specimen was left unimplanted. The implantations were performed by an oto-rhinolaryngologist with over 20 years of experience with cochlear implantation. Two different types of CI-electrodes were used: (i) a relatively rigid perimodiolar electrode array (Contour Advance, CI512, Cochlear Corporation); and (ii) its successor, a slim, flexible perimodiolar electrode array (Slim Modiolar, CI532, Cochlear Corporation). The semi-ring-shaped electrode contacts are approximately 0.3 mm in width and 0.4–0.7 mm in length, depending on the location along the array and the type. A metal alloy with a ratio of 90% platinum to 10% iridium is commonly used for CI-electrodes (Zeng *et al.*, 2008). For one sample, the surgeon had intentionally misplaced the electrode, simulating a scala transition from the scala tympani into the scala vestibuli. To ensure minimal movement of the electrode during transportation, the electrode was cut off at the tail and mechanically fixed within a receptacle drilled in the sinus tympani.
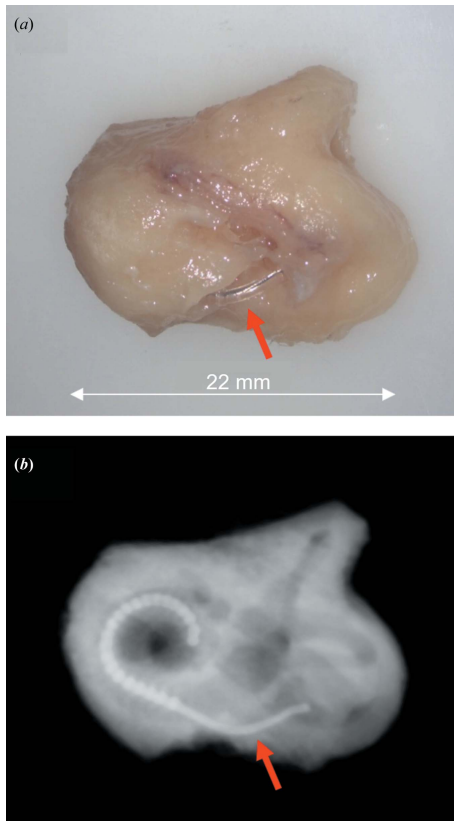
Figure 1
(*a*) Implanted temporal bone specimen as viewed from a Leica M320 surgical microscope and (*b*) a cone-beam computed tomography scan of the same sample. The open-source image-processing software *Icy* (De Chaumont *et al.*, 2012) was used to generate a voxel-intensity-based three-dimensional rendering of the volumetric data in which the locations of the inner structures are faintly revealed. The electrode array can be seen to be fully inserted into the cochlea. The red arrow indicates the tail of the electrode protruding from the sample.

2.3. Synchrotron radiation computed microtomography scans

The SRμCT experiments were performed at the SYRMEP beamline of the Elettra synchrotron facility (Basovizza, Trieste, Italy). This beamline provides, with a bending magnet source at a distance of about 24 m from the sample stage, a laminar-section X-ray beam with a maximum area of approximately 160 mm (h) × 5 mm (v) (Tromba *et al.*, 2010). For the present experiment, the electron storage ring was operating at 2.0 GeV, and a filtered polychromatic X-ray beam (filters: 1.5 mm Si + 1.0 mm Al, mean X-ray energy *ca.* 27 keV) was used to obtain X-rays with a high photon flux, allowing us to reduce the scan duration of the μCT experiments when working at high spatial resolution (pixel size <5 μm) and for X-ray energies >20 keV (Goyens *et al.*, 2018). In order to capture the entire region of interest, two scans per sample were acquired at different vertical positions and then the images were vertically stitched.

Tomographic scans were acquired in propagation-based phase-contrast mode (Cloetens *et al.*, 1997). A total of 1800 projections were acquired over a total scan angle of 360°,

setting the sample off-centre in the field of view (FOV) of the detector (extended horizontal FOV) with an exposure time per projection of 1.5 s. The detector was a water-cooled, 16 bit, sCMOS camera (Hamamatsu C11440-22 C) with a 2048 × 2048 pixel chip coupled with a LSO:Tb scintillator screen (45 μm-thick on top of a 170 μm-thick LSO substrate) through high numerical aperture optics. The effective pixel size was set at 4.95 μm, yielding a maximum FOV of about 20 mm (h) × 4 mm (v). The sample-to-detector distance was set to 0.91 m.

The microtomographic axial slices were reconstructed using the SYRMEP Tomo Project (STP) software suite, custom-developed at Elettra (Brun *et al.*, 2015), applying the filtered back-projection algorithm (Herman, 1980) and then were converted to 16-bit tiff format. The virtual slices were visualized through the *Fiji* software (Schindelin *et al.*, 2012).

Prior to tomographic reconstruction, a single-distance phase-retrieval algorithm, based on the transport of intensity equation (Paganin *et al.*, 2002) was applied to the projection images. We set a value of 200 for the $\delta/\beta = \gamma$ parameter (ratio between the real and imaginary parts of the complex refractive index) after a manual optimization to enhance the contrast of fine anatomical microstructures while minimizing the image blurring. In the supporting information we report some examples of axial slices reconstructed without phase-retrieval and after phase-retrieval using Paganin's algorithm with different γ ratios. These images show how the γ parameter used in this study was optimized and how this affected the image quality. Fig. S7 of the supporting information shows that after application of phase-retrieval, a fivefold improvement could be observed in the contrast-to-noise ratio (Goyens *et al.*, 2018). Application of the algorithm also did not affect the observed thickness of the structures of interest (Figs. S3 and S5).

2.4. Comparator imaging techniques

To evaluate the improvements of SRμCT over clinical imaging as well as over conventional *ex vivo* imaging, cone-beam computed tomography (CBCT) and conventional X-ray microfocus tomography (XμCT) were performed on the same specimens. Clinical CBCT scans were acquired with a NewTom 5G XL CBCT scanner (NewTom, Verona, Italy) and XμCT scans were captured using a SkyScan 1172 scanner (Bruker micro-CT, Kontich, Belgium). The scan parameters used for the CBCT and XμCT experiments are summarized in Tables 1 and 2, respectively.

3. Results and discussion

For all eight temporal bones, SRμCT successfully visualized the intra-cochlear anatomical structures of interest (Fig. 2). The locations of the cochlear scalae, the osseous spiral lamina, the basilar membrane and Rosenthal's canal were evident in the final reconstructions. In addition, the Reissner's membrane (RM), the thinnest membrane of interest which consists of two epithelial cell layers could be visualized. The spatial resolution of the current experimental setup was

short communications

Table 1
Scan parameters for clinical cone-beam computed tomography.

Source voltage (kV)	110
Effective pixel size (mm × mm)	0.125 × 0.125
Sample-to-detector distance (m)	0.3
Source-to-sample distance (m)	0.7
Rotation angle (°)	360
Angular rotation step (°)	0.6
Exposure time per projection (ms)	15
No. of projections	600
Total scanning time (s)	9

Table 2
Scan parameters for conventional X-ray microfocus tomography.

Source voltage (kV)	100
Effective pixel size (μm × μm)	4.98 × 4.98
Sample-to-detector distance (m)	0.1
Source-to-sample distance (m)	0.1
Rotation angle (°)	360
Angular rotation step (°)	0.2
Exposure time per projection (s)	3
No. of projections	1800
Total scanning time (min)	90

evaluated directly from the tomographic slices by considering the thinnest region of RM whose thickness could reliably be measured, and was estimated at approximately 10 μm. The thickness of the RM was measured on a tomographic slice at roughly 2–4 pixels, or about 10–20 μm. Previous studies that employed either histological sectioning (Shibata *et al.*, 2009) or transmission electron microscopy (Fraissinette *et al.*, 1993) to evaluate the structural properties of the RM reported a thickness in the approximate range 4–12 μm. Based on the values in the literature, we conclude that the 10 μm spatial resolution is insufficient to determine the thickness of the membrane. The RM was only found to be present in two of the specimens. Because the membrane is a delicate structure, it was possibly damaged during the processing and fixation of the other samples. In future studies, shortening of the fixation time and employing fresh temporal bones is expected to allow for better preservation of this structure.

Streak artefacts due to the highly absorbing electrode contacts were also observed in the reconstructed images of the implanted samples. However, despite the erroneous voxel intensities in close proximity to the electrode array, it remained possible to identify the location of the intra-cochlear structures with respect to the electrode contacts. Although automatic threshold-based segmentation cannot be achieved with the present data, the image quality allows for precise manual measurements of the electrode locations, which was the main objective of the current study. This is a distinct advantage over conventional XμCT, where in our case the severity of the streaking artefacts was found to be substantially higher (Fig. 3).

The volumetric SRμCT image data were rigidly co-registered to the data acquired from the clinical CBCT system with proprietary image-processing software (*MATLAB* image-processing toolbox, Mathworks, NA). The aligned slices are
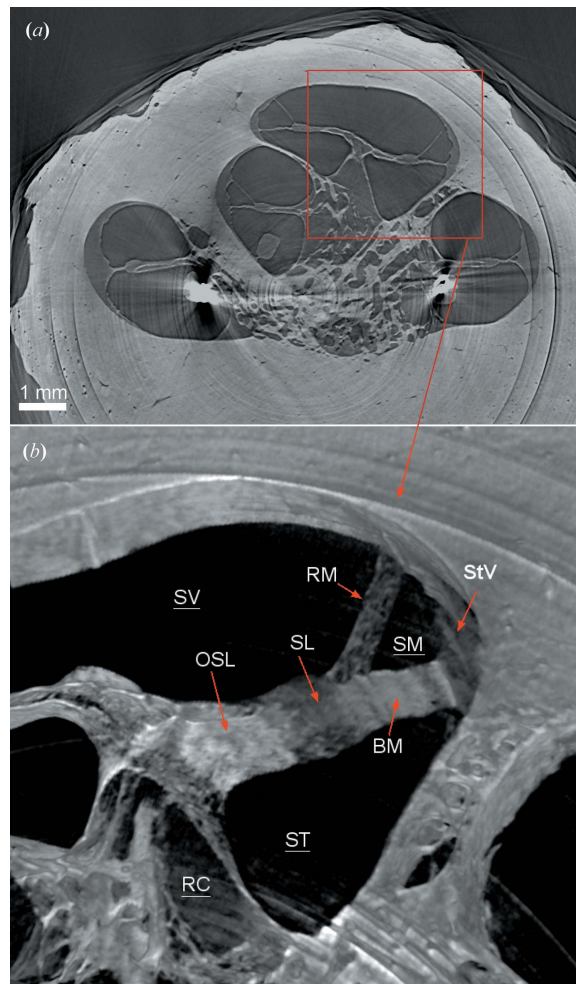
Figure 2
Synchrotron radiation microtomography images of the human implanted cochlea. (*a*) Axial tomographic slice of sample B07. (*b*) Semi-transparent three-dimensional rendering (3D-Rec) generated by setting a manual voxel-intensity threshold on a sub-volume composed of several concatenated slices. The following micro-anatomical structures could be identified and are indicated in (*b*): ST = scala tympani, SV = scala vestibuli, SM = scala media, RC = Rosenthal's canal, OSL = osseous spiral lamina, SL = spiral limbus, RM = Reissner's membrane, BM = basilar membrane, StV = stria vascularis. The partitions of the cochlear duct are underlined. The volume rendering (*b*) was generated using the commercial software *VGStudio Max* (version 2.0; Volume Graphics, Germany). Using the same software, a 3D animation of the same volume was realized (see Movie S1 of the supporting information.

shown in Fig. 4. Fig. 4(*a*) demonstrates a typical atraumatic insertion of the CI-electrode into the scala tympani. Clinical CBCT was unable to visualize the internal structures of the cochlea, whereas synchrotron-based imaging could clearly reveal the separation between the cochlear scalae, thus confirming that the electrode array was positioned fully in the scala tympani. Fig. 4(*b*) instead shows an example of the traumatic dislocation of the CI-electrode in the sample, which had been intentionally induced by the surgeon by misorienting the electrode array during the implantation. SRμCT images showed that the electrode array had translocated into the scala vestibuli, by both rupturing and displacing the basilar membrane.
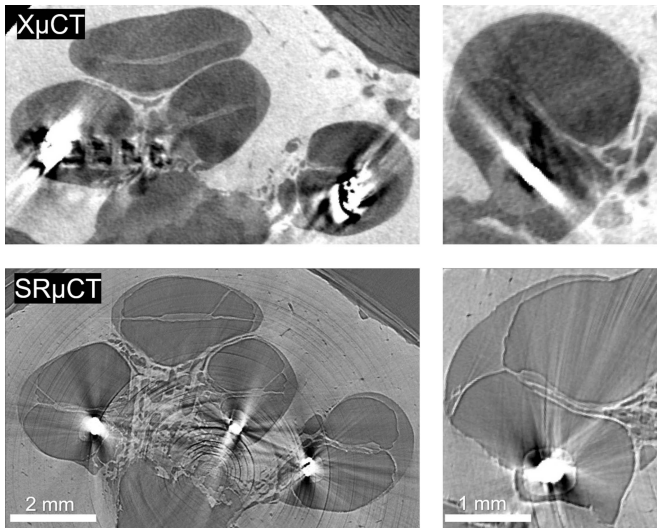
Figure 3
Conventional X-ray microfocus computed tomography (XμCT) versus synchrotron-based computed microtomography (SRμCT). Two different temporal bone samples were scanned, but the volumetric data were manually aligned to display similar cross-sectional views of the cochlea. Streak artefacts due to the highly absorbing platinum contacts were observed with both imaging techniques. However, in SRμCT images, they were substantially less pronounced, allowing for the identification of fine anatomical structures in close proximity to the electrode contacts.
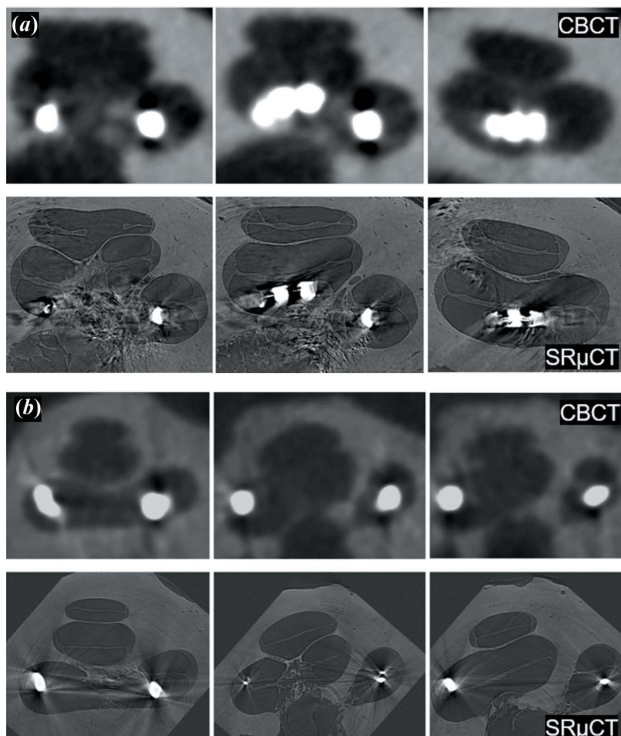

Figure 4
Two implanted cochleae visualized with clinical cone-beam computed tomography (CBCT) and synchrotron radiation computed microtomography (SRμCT). The images were rigidly co-registered with image-processing software to accurately align the volumetric datasets. (*a*) Atraumatic insertion into the scala tympani (the inferior partition of the cochlear duct), (*b*) traumatic electrode array dislocation into the scala vestibuli (the superior partition). Though clinical CBCT was unable to, SRμCT could clearly reveal the separation between the cochlear scalae, thus confirming the scalar electrode location.

4. Conclusions and outlook

The results presented in this report demonstrate that, by using propagation-based phase-contrast synchrotron X-ray micro-tomography, it is possible to visualize both the electrode contacts and the intra-cochlear anatomical structures simultaneously, even when imaging cochleas implanted with a perimodiolar electrode array. However, the presence of the highly absorbing, closely spaced platinum–iridium contacts still resulted in significant streak artefacts that could interfere with the accurate analysis of the CI-electrode positions. Therefore, our future studies will focus on further reducing the contribution of the CI-related metal artefact. In particular, we will investigate the capabilities of synchrotron-based imaging in monochromatic beam mode and at higher beam energies, *ca.* 40 keV, in order to improve the X-ray transmission while maximally preserving the soft tissue contrast within the specimen. We will also focus on the development of an application-specific tomographic reconstruction algorithm to reduce the metal artefact.

References

Brun, F, Pacilè, S, Accardo, A., Kourousias, G,, Dreossi, D., Mancini, L., Tromba, G. & Pugliese, R. (2015). *Fund. Inform.* **141**, 233–243.

Chakravorti, S., Noble, J. H., Gifford, R. H., Dawant, B. M., O'Connell, B. P., Wang, J. & Labadie, R. F. (2019). *Otol. Neurotol.* **40**, 617–624.

Cloetens, P., Pateyron-Salomé, M., Buffière, J. Y., Peix, G., Baruchel, J., Peyrin, F. & Schlenker, M. (1997). *J. Appl. Phys.* **81**, 5878–5886.

De Chaumont, F., Dallongeville, S., Chenouard, N., Hervé, N., Pop, S., Provoost, T., Meas-Yedid, V., Pankajakshan, P., Lecomte, T., Le Montagner, Y., Lagache, T., Dufour, A. & Olivo-Marin, J. C. (2012). *Nat. Methods*, **9**, 690–696.

Elfarnawany, M., Alam, S. R., Rohani, S. A., Zhu, N., Agrawal, S. K. & Ladak, H. M. (2017). *J. Microsc.* **265**, 349–357.

Fraissinette, A. de, Felix, H., Hoffmann, V., Johnsson, L. G. & Gleeson, M. J. (1993). *Orl*, **55**, 68–72.

Goyens, J., Vasilopoulou-Kampitsi, M., Claes, R., Sijbers, J. & Mancini, L. (2018). *J. Anat.* **233**, 770–782.

Herman, G. T. (1980). *Image Reconstruction from Projections: The Fundamentals of Computerized Tomography*. New York: Academic Press.

Holden, L. K., Finley, C. C., Firszt, J. B., Holden, T. A., Brenner, C., Potts, L. G., Gotter, B. D., Vanderhoof, S. S., Mispagel, K., Heydebrand, G. & Skinner, M. W. (2013). *Ear Hear.* **34**, 342–360.

short communications

Iso-Mustajärvi, M., Matikka, H., Risi, F., Sipari, S., Koski, T., Willberg, T., Lehtimäki, A., Tervaniemi, J., Löppönen, H. & Dietz, A. (2017). *Otol. Neurotol.* **38**, e327–e334.

Iyer, J. S., Zhu, N., Gasilov, S., Ladak, H. M., Agrawal, S. K. & Stankovic, K. M. (2018). *Biomed. Opt. Expr.* **9**, 3757.

Johnson, S. B., Cureoglu, S., O'Malley, J. T. & Santi, P. A. (2014). *Otol. Neurotol.* **135**, 1.

Kawano, A., Seldon, H., Clark, G. M., Ramsden, R. T. & Raine, C. H. (1998). *Acta Otolaryngol.* **118**, 313–326.

Li, H., Schart-Morén, N., Rohani, S. A., Ladak, H. M., Rask-Andersen, H. & Agrawal, S. (2019). *Ear Hear.* **41**, 173–181.

Paganin, D., Mayo, S. C., Gureyev, T. E., Miller, P. R. & Wilkins, S. W. (2002). *J. Microsc.* **206**, 33–40.

Rau, T. S., Würfel, W., Lenarz, T. & Majdani, O. (2013). *Int. J. CARS*, **8**, 481–509.

Rohani, S. A., Iyaniwura, J. E., Zhu, N., Agrawal, S. K. & Ladak, H. M. (2018). *J. Microsc.* **273**, 127–134.

Saeed, S. R., Selvadurai, D., Beale, T., Biggs, N., Murray, B., Gibson, P., Risi, F. & Boyd, P. (2014). *Otol. Neurotol.* **35**, 1338–1344.

Schart-Morén, N., Agrawal, S. K., Ladak, H. M., Li, H. & Rask-Andersen, H. (2019). *Ear Hear.* **40**, 393–400.

Schindelin, J., Arganda-Carreras, I., Frise, E., Kaynig, V., Longair, M., Pietzsch, T., Preibisch, S., Rueden, C., Saalfeld, S., Schmid, B., Tinevez, J. Y., White, D. J., Hartenstein, V., Eliceiri, K., Tomancak, P. & Cardona, A. (2012). *Nat. Methods*, **9**, 676–682.

Shaul, C., Dragovic, A. S., Stringer, A. K., O'Leary, S. J. & Briggs, R. J. (2018). *J. Laryngol. Otol.* **132**, 1000–1006.

Shibata, T., Matsumoto, S., Agishi, T. & Nagano, T. (2009). *Am. J. Otolaryngol.* **30**, 112–120.

Sun, Q., Chang, K. H., Dormer, K. J., Dyer, R. K. & Gan, R. Z. (2002). *Med. Eng. Phys.* **24**, 595–606.

Tromba, G., Longo, R., Abrami, A., Arfelli, F., Astolfo, A., Bregant, P., Brun, F., Casarin, K., Chenda, V., Dreossi, D., Hola, M., Kaiser, J., Mancini, L., Menk, R. H., Quai, E., Quaia, E., Rigon, L., Rokvic, T., Sodini, N., Sanabor, D., Schultke, E., Tonutti, M., Vascotto, A., Zanconati, F., Cova, M., Castelli, E. & Siu, K. K. W. (2010). *AIP Conf. Proc.* **1266**, 18–23.

Zeng, F. G., Rebscher, S., Harrison, W. V., Sun, X. & Feng, H. (2008). *Biomed. Eng.* **1**, 115–142.